DOI: 10.1002/ejic.201100165

Tetrahedratic Mesophases, Ambidextrous Chiral Domains and Helical Superstructures Produced by Achiral 1,1′-Disubstituted Ferrocene Derivatives

Eun Ho Kim,[a] Oleg Nikolaevich Kadkin,*[a,b] So Yeon Kim,[a] and Moon-Gun Choi*[a]

Keywords: Liquid crystals / Mesophases / Ferrocene / Chirality / Helical structures

A series of symmetrically and asymmetrically 1,1′-disubstituted mesogenic ferrocene derivatives exhibiting nonconventional lamellar and nematic phases has been synthesized. Liquid-crystal properties of these compounds were investigated by polarizing optical microscopy (POM), thermal analysis (DSC) and X-ray scattering methods (XRD). XRD patterns and optical textures of the mesophases have a complex appearance, standing apart from the signatures of previously classified liquid crystals. The most important features of the new mesophases are their spontaneous separation into large macroscopic chiral domains of opposite handednesses, intricate helical and myelinic supramolecular structures and a few signs of possible optical biaxiality. A reasonable explanation of these findings can be drawn from the tetrahedral liquid crystal order. Free rotation of the cyclopentadiene rings in the ferrocene moiety around their normal axis makes viable bent conformations of the rod-like molecules and further stabilization of the conformational enantiomers through assembly into tetrahedral molecular associates. Thus, fundamentally new types of mesophases arise from such a molecular arrangement. In addition, a nontrivial case of mixed packing of bent and nonbent molecules into columnar mesophases was detected in one of the symmetrically substituted ferrocene derivatives. Basic relationships between mesomorphic properties, supramolecular organization and chemical structures of the ferrocenomesogens have been outlined.

Introduction

There are a number of classifications of liquid crystals or mesophases depending on their internal molecular organization.[1] Introducing chirality into mesogenic molecules induces a variety of helically arranged mesophases.[2] Sometimes spontaneous symmetry breakage occurs in supramolecular systems, crystal and liquid-crystal phases comprising achiral molecules without stereogenic centres.[3] For instance, interesting cases of cooperative chirality have been observed in hydrogen-bonded liquid crystals[4] and bent-core mesogenic systems.[5] In this work a new type of spontaneously chiral mesophases from nonchiral entities associated with the tetrahedral arrangement is reported.

A theoretical possibility of tetrahedral symmetry in liquid crystals was first introduced by Fel.[6] The topic was discussed later for its potential relevance to banana mesophases.[7,8] Lubensky and Radzihovsky took into consideration some variations of the tetrahedral mesophases in addition to the true tetrahedral mesophase, T, that is, the N_T mesophase with uniaxial distortion and the spontaneously chiral biaxial variant $(N_T + 2)^*$ (Figure 1). They also predicted layered analogs of the above fluid phases derived from the combination of the tetrahedral symmetry groups with a smectic order. Pleiner et al. introduced the concept of columnar tetrahedral mesophases,[8b] discussed splay-bend textures in relation to terahedral arrangements[8c] and the possibility of tetrahedral distortions.[8d] In accordance with these theoretical considerations, a tetrahedral order may lead to ambidextrous chirality, optical biaxiality and, possibly, to ferroelectric or antiferroelectric behaviour akin to banana mesophases.

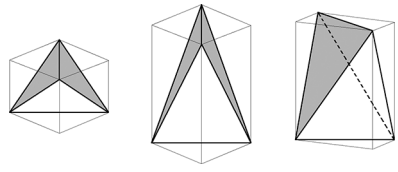

Figure 1. Schematic representation of the tetrahedral symmetry groups, T – a true tetrahedron, N_T – a uniaxially distorted tetrahedron, $(N_T + 2)^*$ – a biaxially distorted tetrahedron.[7]

We have previously suggested a tetrahedral arrangement to explain bulk asymmetry in nonchiral asymmetrically 1,1′-disubstituted ferrocenomesogens.[9] In principle, both symmetrically and asymetrically substituted ferrocenes can exhibit tetrahedral mesophases. Disubstituted ferrocenomesogens with their freely rotating central core are exceptionally suited for the formation of elementary units of the $(N_T + 2)^*$ type. Thus, in ferrocene derivatives we have a

[a] Department of Chemistry, Yonsei University
50 Yonsei-ro, Seodaemun-gu, Seoul 120-749, Korea
Fax: +82-2-364-7050
E-mail: onk@yonsei.ac.kr
choim@yonsei.ac.kr
[b] Department of Physical and Colloid Chemistry, Kazan State Technological University
68 K. Marks Str., 420015 Kazan, Russian Federation
Fax: +7-843-2366523
E-mail: oleg.kadkin@bk.ru

Supporting information for this article is available on the WWW under http://dx.doi.org/10.1002/ejic.201100165.

serendipitous condition when the free rotation of the cyclopentadienyl rings allows the adoption of chiral conformations in line with a weak chiral field, and – most importantly – such conformations can be locked and stabilized by coupling with neighbour conformers of the same handedness into tetrahedral dimers.

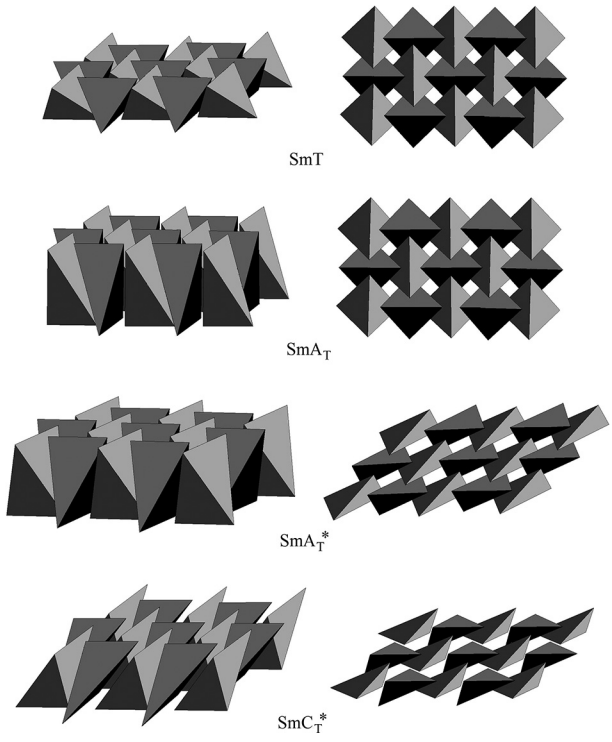

Figure 2. Various possible types of the tetrahedral lamellar mesophases: SmT (layered packing of true tetrahedra), SmA$_T$ (layered packing of uniaxially distorted tetrahedra), SmA$_T$* (layered heterochiral packing of biaxially distorted tetrahedra), SmC$_T$* (layered heterochiral packing of skewed tetrahedra). Appropriate 3D projections of the smectic layers are illustrated on the left, and a view from the top of the layers is shown on the right.

We propose herein several variations of the layered arrangement of the tetrahedral elementary units depending on their geometry as shown in Figure 2. The tetrahedral mesophases illustrated appear to be optically isotropic, with the exception of the SmC$_T$* mesophase. It should be noted that biaxially distorted and skewed tetrahedra are chirally degenerate. As both optical antipodes can be formed, we illustrate here the heterochiral packing of such units. However, chiral segregation may cause twisted deformations of the lamellar layers, and – as a consequence – unusual optical textures can be observed with a polarizing microscope. The results reported herein demonstrate that 1,1′-disubstituted ferrocenes can form tetrahedrally organized nematic and smectic mesophases. Tetrahedral order explains the complex XRD patterns, chiral domains and helical supramolecular aggregates. In a more general context, understanding the mechanisms of asymmetric induction from achiral molecules is a significant step towards the elucidation of the origin of dominant optical isomerism in natural organic compounds.

Results and Discussion

Syntheses and Characterization

Scheme 1 illustrates the chemical structures of the ferrocene-containing liquid crystals synthesized. We have reported a method for preparing [4-(*trans*-4-alkylcyclohexyl)-2,3-difluorophenyl]boronic acid and asymmetrically disubstituted ferrocene **3a** previously.[9] The use of different aldehydes afforded two more asymmetrically substituted Schiff bases **2** and **3b**. Symmetrical 1,1′-disubstituted ferrocenes **1a** and **1b** were prepared by a standard Suzuki–Miyaura crosscoupling with (dibromophenyl)ferrocene and the appropriate boronic acids with five and ten carbon atoms in the terminal alkyl substituent. (Dibromophenyl)ferrocene was obtained in 20% yield from commercially available

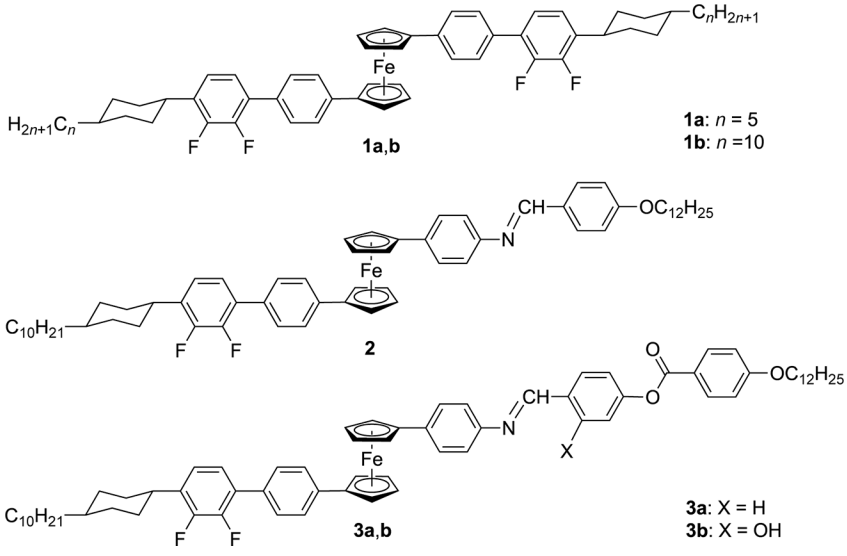

Scheme 1. Symmetrically and asymmetrically 1,1′-disubstituted ferrocenes **1**–**3**.

ferrocenediboronic acid and a four-fold excess of 1,4-dibromobenzene.[10] Spectral characteristics and elemental analyses unambiguously confirmed the structures of **1**–**3**.

Thermo-Optical Behaviour and XRD Studies

Phase transitions in compounds **1a**, **1b**, **2**, **3a** and **3b** were investigated by POM, DSC and XRD. The results are summarized in Table 1.

Compound **1a** exhibited a nematic mesophase with unusual POM textures. Nonbirefringent dark nematic droplets with slightly birefringent edges developed upon cooling from the isotropic liquid state, which grew eventually to a dark mesophase (Figure 3). However, in the perimeter areas some helical chiral droplets and birefringent stripes were observed. On average, both left- and right-handed droplets are equally distributed. The stripes also appeared to have a chiral arrangement as their birefringence remained unaffected under uncrossed nicols. Further cooling led to some transformation of the boundaries of the dark nematic domains, which showed periodic bright nodes at approximately equal intervals (Figure 3d).

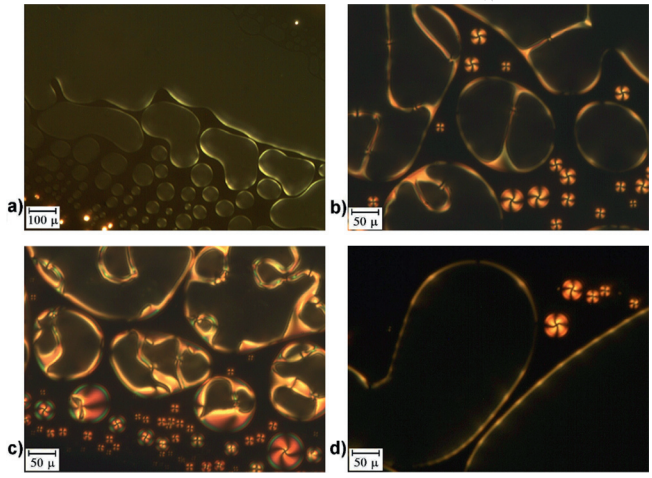

Figure 3. Microphotographs of the N_T* mesophase of **1a** between untreated microscope slides: (a) dark nematic droplets just after transition from the isotropic liquid state at 252 °C; (b) development of helical droplets and birefringent stripes in the perimeter areas of the sample at 245 °C; (c) further growing of chiral formations at 240 °C; (d) boundaries of dark areas of the N_T* mesophase with periodic nodes at 240 °C.

The observations described above suggest a nontrivial internal organization of the examined nematic mesophase. We explain the mesoscopic chirality found in **1a** by a special arrangement of the molecules involving tetrahedral dimer entities. Accordingly, several coincidentally occurring conditions in the ferrocene derivatives with π-conjugated adjacent aromatic rings give rise to this type of molecular organization. First, the bent conformers may exist because of free rotation of the cyclopentadienyl rings around their normals. Second, the bent conformers can be interlocked

Table 1. Phase-transition parameters of compounds **1a**, **1b**, **2**, **3a** and **3b** determined by POM, DSC and selected XRD data.

Compound	Phase transition[a]	T [°C] (ΔH [kJ mol^{-1}]) Heating course	Cooling course	d spacing value [Å] (T [°C])
1a	Cr_1–Cr_2	149.4 (15.6)	–[e]	–
	Cr_2–N_T*	201.6 (40.2)	185.7 (–10.4)	–
	N_T*–I	253.0 [b]	252.0 [b]	–
1b	Cr_1–Cr_2	154.5 (0.9)	–[e]	43.0, 5.6, 5.5, 4.6 (25)
	Cr_2–Col_{mix}	162.9 (9.3)	–[e]	44.1, 5.7, 5.6, 5.1, 4.7, 3.9 (161)
	Col_{mix}–SmA_T*	181.5 (13.3)	183.1 (–8.7)	73.6, 43.0, 36.8, 6.0[f] (177)
	SmA_T*–N_T*	225.9 (2.4) [c]	225.5 (–1.8) [c]	49.0, 5.1[f] (195)
	N_T*–I	227.6 (2.4) [c]	227.6 (–1.8) [c]	45.2, 5.4[f] (226)
2	Cr_1–Cr_2	113.0 (2.8)	–[e]	46.5, 7.1, 6.6, 6.1, 5.2, 4.7, 4.6, 4.4, 4.3, 3.7 (25)
	Cr_2–SmA_T*	194.6 (30.0)	193.6 (–29.5)	47.7, 7.1, 6.6, 6.1, 5.3, 4.8, 4.7, 4.5, 4.4 (180)
	SmA_T*–N_T*	204.9 (2.0) [c]	204.4 (–1.2) [c]	46.9, 7.2, 5.4, 4.8, 4.5 (200)
	N_T*–I	205.9 (4.0) [c]	205.8 (–3.5) [c]	45.3, 5.0[f] (205)
3a	Cr_1–Cr_2	91.9 (2.7)	83.4 (–2.6)	46.0,[g] 39.2,[g] 34.1,[g] 4.4[h] (25)
	Cr_2–SmC_T*	203.4 (23.9)	200.8 (–20.2)	48.0, 5.3, 4.9, 4.5 (200)
	SmC_T*–N_T*	215.5 (0.4)	212.2 (–0. 6)	48.0, 5.4, 4.8, 4.5 (210)
	N_T*–I	271.6 (1.6)	271.4 (–1.9)	48.0, 5.1[f] (220)
3b	Cr_1–Cr_2	147.1 (4.1)	–[e]	38.8, 7.3, 7.1, 6.5, 5.4, 5.3, 4.9, 4.8, 4.5, 4.3, 3.3 (25)
	Cr_2–Cr_3	175.5 (6.6)	–[e]	39.9, 7.3, 7.0, 5.5, 5.4, 4.9,[i] 4.6[i] (155)
	Cr_3–SmC	205.5 (19.8)	192 (–10.5)	48.7, 5.4, 4.9, 4.8, 4.6[i] (185)
	SmC–SmA_T*	225.0 (0.0) [d]	225.0 (0.00) [d]	54.9, 5.0[f] (215)
	SmA_T*–N_T*	279.9 (1.7)	–	50.6, 5.1[f] (230)
	N_T*–I	286.9 (3.5)	282.5 (–0.1)	42.1,[i] 5.4[f] (282)

[a] Cr = crystal, Col_{mix} = columnar packing of the mixture of bent and nonbent conformers, SmA_T* = tetrahedral smectic A, SmC_T* = tetrahedral smectic C, N_T* = tetrahedral nematic, I = isotropic liquid phases. [b] Determined by POM. [c] In the case of close phase transitions, enthalpy values are estimated visually from the total value of two fused DSC peaks. [d] In fact a second-order phase transition, which is identified by changes in the POM texture and a layer spacing distance in X-ray scattering experiments. [e] Crystallization peaks are absent in the cooling course at both scanning rates 1 °C min^{-1} and 5 °C min^{-1}. [f] Very broad reflection with the rough maximum indicated. [g] Multiple reflections, the most intense peak is given. [h] Numerous additional weak reflections in the wide-angle region are not given. [i] Broadened reflection.

due to a stepwise configuration and straightforward plain-to-plain alignment of the aromatic rings of two molecules favouring their efficient π-π stacking interactions. Computerized modelling gave an energy drop of around 60 kJ mol^{-1} when the interlocked structures are compared with two stacked *transoid* conformers. Third, the bent conformers have an enantiomeric relationship, and – most importantly – the mirror antipodes cannot form interlocked dimers (Figure 4). This can be compared with a handshake; it is common for people to shake right hands and grasping a right hand with a left hand is inconvenient. Thus, this "handshake effect" leads to self-assembly, whereby the next molecule adopts the same handedness under the influence of the chiral field from the first pair of homochiral conformers. Thus, randomly distributed mesoscopic and macroscopic chiral domains of both handednesses can develop in the material.

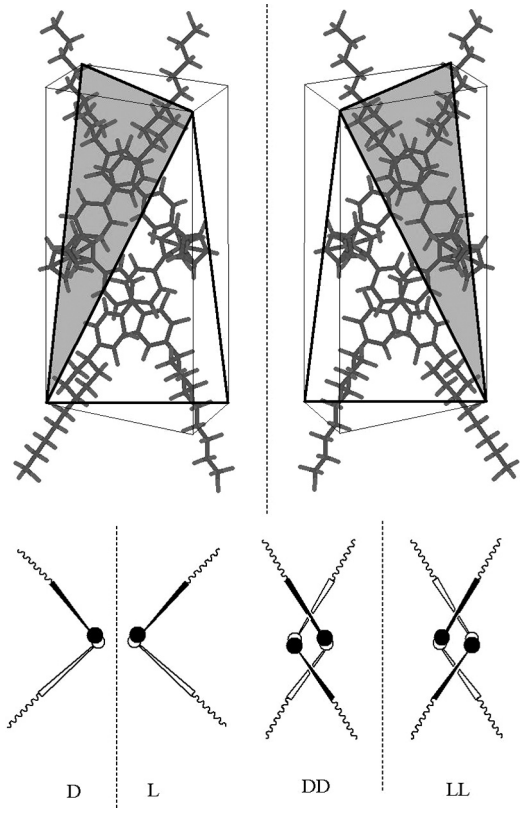

Figure 4. Molecular models of tetrahedratic associates in **1a** and mirror relationships in the bent conformers.

Remarkably, lengthening of the terminal alkyl chains to ten carbon atoms gave rise to mesomorphic behaviour of **1b** (see Table 1). A crystal-to-crystal polymorphic transition and three mesophases were detected by DSC and POM. Unexpectedly, the mesophase with a columnar arrangement was found in this apparently rod-like mesogen. An appropriate mesophase texture was detected by POM on the cooling course from the lamellar mesophase of **1b** (see Figure 5a). Three intense peaks were observed in the small-angle region of XRD patterns of **1b** at 170–180 °C (Figure 6). The most intense (100) reflection far exceeds the length 56 Å for a *transoid* conformation of **1b** obtained by computer modelling (see Table 1). The most realistic packing, which may give rise to this unusual periodic distance, seems to be a parquet-like arrangement of the clusters of

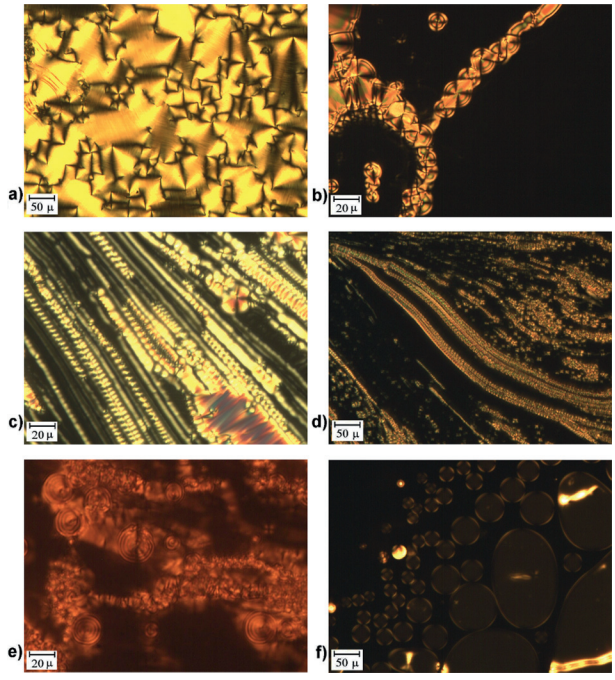

Figure 5. Microphotographs of POM textures of **1b** between untreated microscope slides: (a) focal-conic texture of the Col_{mix} mesophase at 175 °C; (b) conglomerates of focal-conic defects of the SmA_T* mesophase at 220 °C; (c) helical strands obtained by stressing a dark texture of the SmA_T* mesophase; (d) myelinic formations at 205 °C; (e) example of an SmA_T* texture in a thick sample (ca. 50 µm); (f) dark droplets of the N_T* mesophase at 226 °C on cooling from the isotropic liquid state.

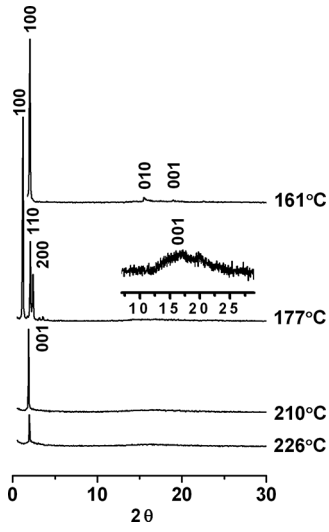

Figure 6. XRD patterns of **1b** at different temperatures and thermodynamic phase states.

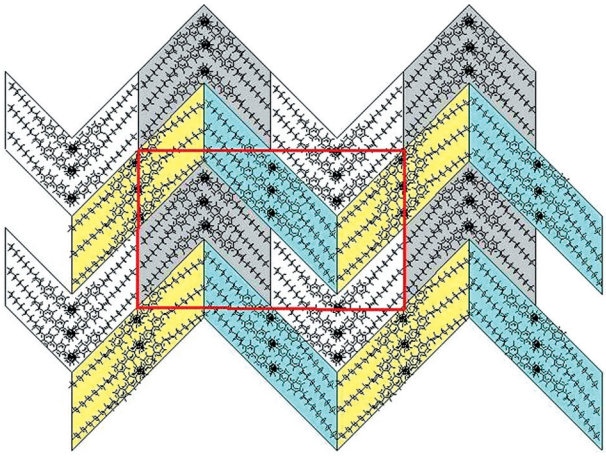

Figure 7. Computerized models illustrating a possible molecular arrangement of **1b** in the rectangular 2D periodic lattice with the parameters *a* and *b*.

bent and nonbent conformers (see Figure 7). The 2D periodic lattice is formed by combined rectangular packing of two different kinds of molecular bunches, that is rhomboid and V-shaped. The number of molecules in one elementary rectangular cell can be calculated by applying the formula:

$n = a \times b \times h \times (N_A/M) \times \rho$

where *a* and *b* are interlayer spacing distances between the (100) and (010) layers, respectively, *h* is a stacking distance, and ρ is a density taken as ca. 1.0 $g\,cm^{-3}$. Considering the 2D lattice parameters *a* and *b* as 73.6 Å and 43.0 Å, respectively, and a stacking parameter of ca. 0.6 Å from the XRD experiments, a calculated number of molecules *n* between 11 and 12 was obtained. Thus, the calculated value is in agreement with the model in Figure 7, and the modelled molecules of **1b** fit perfectly in the suggested 2D periodic lattice.

The XRD layer-spacing distance obtained in the temperature region corresponding to the smectic mesophase of **1b** is essentially lower than the full length of the molecule. Optical defects in dark areas, resembling the SmA mesophase, were observed by polarized light microscopy (Figure 5b–e). Myelinic patterns and complex cord-like superstructures, which were found in this mesophase, are reminiscent of mesophases derived from chiral compounds. Furthermore, the nematic mesophase with the features described for **1a** was also observed for **1b**, although within a small temperature interval (Figure 5f). Considering these unusual optical textures and the XRD interlayer spacing distance, we suggest a liquid-crystalline order of the tetrahedral molecular dimers discussed above. The computed length of the tetrahedral dimers agrees with the relevant spacing parameter of the smectic layers, which was found to be 49.0 Å from the XRD experiments.

Further examples of the tetrahedral mesophases were obtained in asymmetrical 1,1′-disubstituted ferrocene **2** with comparable substituent lengths. In DSC curves of **2** four peaks can be identified. The first peak at 114 °C reveals a crystal-to-crystal polymorphic transition with a relatively small heat effect (Table 1). The second peak with a significant enthalpy value indicates a transition to the smectic mesophase. Smectic-to-nematic and nematic-to-isotropic liquid transitions are characterized by a relatively small summarized heat absorption of 6.01 $kJ\,mol^{-1}$. On the cooling course all these phase transitions are presented on DSC curves in the reverse order with some supercooling effects in the more ordered phases. In thick layers (ca. 20 μm), the mesophase of a smectic type showed myelin-like formations against a dark background (Figure 8a, b) and undulating coloured stripes (Figure 8c). These observations suggest a TGB-like (TGB = twist-grain boundary) helical twist of the smectic plains, which is generally connected with the presence of elements of chirality at the molecular level.[11] Thus, it appears that chiral segregation at the mesoscopic level occurs in achiral compound **2**. The tetrahedral dimers and adoption of bent conformations of the same handedness by neighbour molecules can provide a rational mechanism for the transfer of chirality to a mesoscopic level in **2**. In line with these considerations we assign the observed mesophases in **2** to tetrahedral smectic A with the notations SmA_T* and nematic N_T* (Figure 8d).

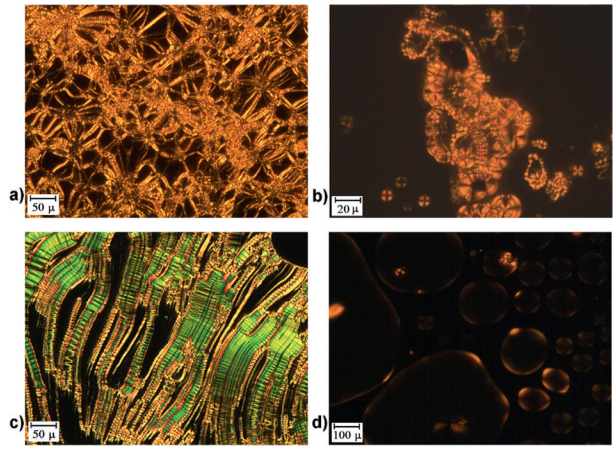

Figure 8. Microphotographs of POM textures of **2** between untreated microscope slides: (a) myelin-like texture of the SmA_T* mesophase at 198 °C on melting from the crystal state; (b) intricate defects in a dark texture of the SmA_T* mesophase at 200 °C; (c) undulated coloured stripes obtained by stressing a dark texture of the SmA_T* mesophase; (d) dark droplets of the N_T* mesophase at 205 °C.

Another intriguing behaviour of **2** is the relatively complex XRD pattern of the SmA_T* mesophase in the wide-angle region, which could be misinterpreted as a crystal state (see Figure 9). High fluidity of the mesophase undoubtedly indicates its liquid-crystalline character. In addition, the SmA_T* phase is separated from the solid-crystal state by a relatively high heat effect of 30 $kJ\,mol^{-1}$, and a smectic-to-nematic transition is characterized by a small enthalpy value of ca. 0.5 $kJ\,mol^{-1}$. Furthemore, as in previous cases, the SmA_T* and N_T* mesophases of **2** show large optically isotropic areas. We suggest that dark areas arise from the heterochiral packing of the bimolecular tetrahedra as shown in Figure 2. In this case a complex wide-angle X-ray scattering pattern is a result of the regular packing of the

terahedral assemblies within the smectic layers. A further argument in favour of the tetrahedral arrangement in the SmA_T* mesophase of **2** is connected with the exceptionally persistent interlayer distance of around 47 Å determined from the XRD measurements. Miscibility studies of the melts of **1b** and **2** in the range of 198–202 °C confirmed the equality of the suggested SmA_T* mesophase in both cases, though reflection signals of **1b** in the wide-angle region are less expressed.

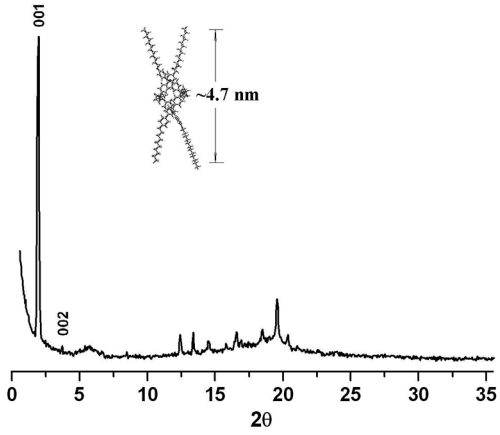

Figure 9. X-ray diffraction pattern of the SmA_T* phase of **2** obtained at 200 °C, and computerized model of the tetrahedral molecular associate.

Compound **3a** has been reported previously.[9] The tilted mesophase assigned as SmC_T* can be explained satisfactorily by a skewed version of the tetrahedral molecular associates causing the emergence of large homochiral domains (Figure 10). As for the broad nematic mesophase in **3a**, it has the same traits as the N_T* phase in the analogs describe above. There are some additional observations of ribbon-like defects within a schlieren texture and multicoloured stripes in the N_T* mesophase (Figure 11a, b), which are of considerable interest in pointing out unconventional internal organization of this nematic mesophase. In homeotropically aligned thin cells filled with **3a** in the N_T* state, the second optical axis can be distinguished by rotation of the crossed polarizers with respect to the sample (Figure 11c, d).

In view of the multifaceted geometry of the tetrahedral mesophases, scrutiny of possible biaxial phenomena in these compounds may not be limited just to regarding the tetrahedral molecular dimers as board-shaped mesogens. The tetrahedral mesophases can be considered as a superposition of two mesophases with two correlated orientation directors since individual mesogenic molecules in the tetrahedral dimers can still be treated as independent entities (Figure 12 left). Accordingly, several preferential orientation directors can be drawn from such a consideration in the case of restricted rotation of the associated molecules. Furthermore, the biaxial symmetry of tetrahedral mesophases becomes unconventional as the angles between orientational axes vary from the standard orthorhombic case. Theoretical models of biaxial liquid crystals with alternative symmetries have been investigated by a number of authors.[12] Indeed, all the above motifs are also related to the biaxial organization of racemic mixtures of bimolecular tetrahedra. Additional complications may arise from chiral segregation and a possible helical twist of the orientational directors in the mesophases observed. Although the experimental evidence of optical biaxiality is not straightforward, there is a high probability of optical biaxiality in these tetrahedral mesophases.

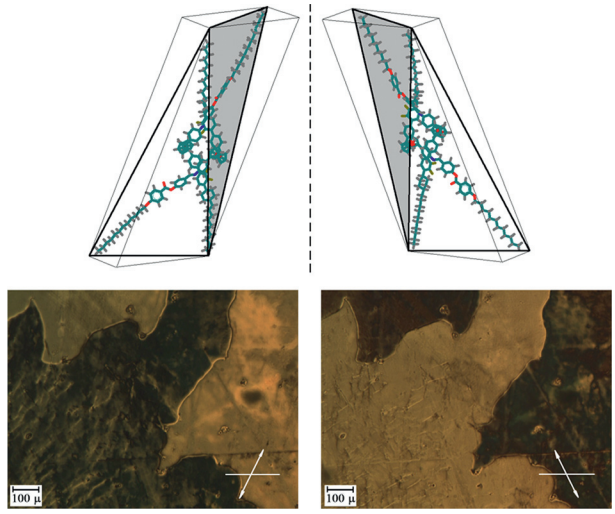

Figure 10. Molecular models of **3a** forming skewed tetrahedra with an enantiomeric relationship and observation of the switching brightness of large chiral domains in the SmC_T* state at 205 °C by slight rotation (ca. 10°) of the analyzer from the crossed position.

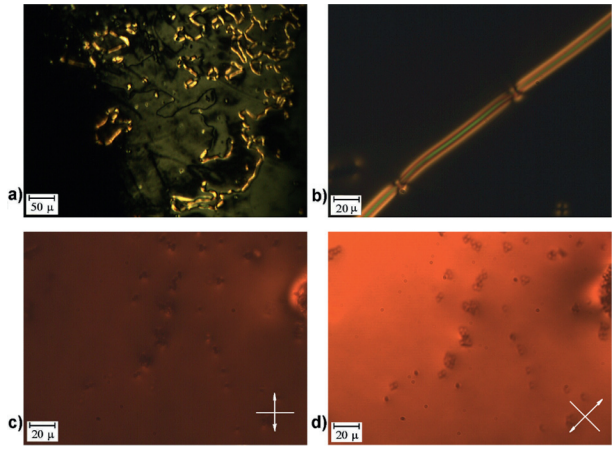

Figure 11. Microphotographs of the N_T* mesophase of **3a**: (a) surface defects with dark threads and birefringent ribbons; (b) example of a multicoloured striped defect; (c), (d) discrimination of the second optical axis by rotation of a 4 µm homeotropic cell with polyimide-coated surfaces around the crossed polarizers; temperature of the sample 220 °C, polymer spacers as round dots.

Introducing the lateral hydroxy substituent in the *ortho* position to the imine group in compound **3b** with disparate arm substituents leads to steric hindrance, which counters the formation of skewed tetrahedral dimers expected by analogy to **3a** (Figure 12). Accordingly, there was no SmC_T* mesophase with homochiral domains observed in

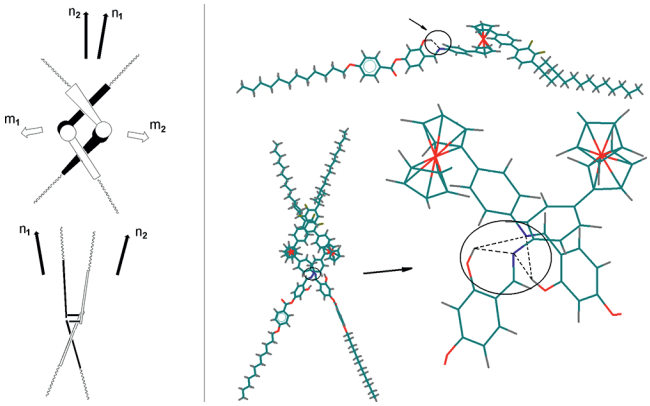

Figure 12. Different orientational axes if the mesogenic molecules in the tetrahedral dimers are considered independently (left); molecular models of **3b** illustrating a steric hindrance for skewed tetrahedral dimers caused by the hydroxy group and nonskewed tetrahedral dimers linked by multiple hydrogen bonds (right).

3b, but the conventional smectic C mesophase with tilted layers comprising rod-like *transoid* conformers. The SmC mesophase was identified by a characteristic marbled-schlieren texture in POM studies (Figure 13a). Strong diffraction from the smectic layers was found in the small-angle region by X-ray scattering (see Table 1). The calculated length of the *transoid* conformation of **3b** considerably exceeds the experimental interlayer spacing distance between smectic lamellas (61 vs. 55 Å). Conversely, the spacing parameter of the tetrahedral SmC_T* mesophase of **3a** with a comparable chemical structure is significantly less (48 vs. 55 Å). Hence, the conventional smectic C arrangement was concluded for the mesophase observed in **3b**. A tilt angle of the long axes of molecules with respect to the orthogonal position has been estimated from the XRD data as 25°.

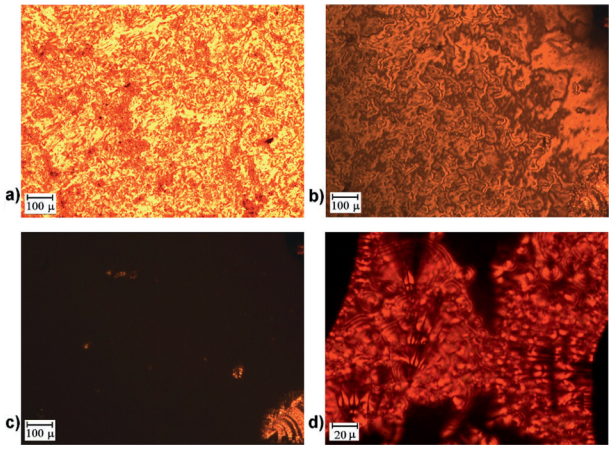

Figure 13. Microphotographs of POM textures of **3b**: (a) marble-schlieren texture of the SmC mesophase at 210 °C; (b), (c) change of a schlieren texture of the smectic C to a homeotropic texture of the SmA_T* at 225 °C; some myelinic formations, which are seen in the right bottom corner in both of the pictures, are unchanged during the phase transition; (d) area with birefringent defects of the SmA_T* mesophase.

Although the skewed tetrahedral formations are suppressed, nonskewed tetrahedral dimers are still successfully produced due to the interlinked hydrogen bonds between the azomethine and hydroxy groups (Figure 12). As the result of developing nonskewed tetrahedral dimers, a phase transition without detectable heat effect was found at 225 °C, when an SmC schlieren texture changed to a dark texture of the orthogonal smectic mesophase (Figure 13b, c). An intriguing point is that the interlayer spacing distance in this orthogonal smectic (50 Å) is less than in the tilted SmC mesophase. The observed layer shrinkage after transition from the tilted to orthogonal smectic is abnormal at first glance but can be explained by the tetrahedral SmA_T* mesophase by analogy with previous cases. Some areas of the SmA_T* mesophase of **3b** also show unconventional optical textures under a polarized light microscope (Figure 13d). Upon further heating, the SmA_T* mesophase transformed to the dark N_T* mesophase with the same features as seen in other compounds of this series.

Conclusions

A fundamentally new type of molecular organization in the liquid-crystal phases associated with tetrahedral symmetry was applied to explain the unusual thermal behaviour of symmetrically and asymmetrically 1,1′-disubstituted ferrocene derivatives. The compounds showed a variety of unconventional mesophases depending on the chemical structure of the ferrocene substituents, which were assigned as tetrahedral lamellar SmA_T*, SmC_T* and nematic N_T* mesophases. The main features of the new mesophases include spontaneously developed macroscopic and mesoscopic homochiral domains, complex supramolecular formations, some symptoms of optical biaxiality and optically isotropic appearance in heterochiral areas. The optical phenomena, chirality and complex XRD features of the new mesophases can be construed by involvement of the biaxially distorted and skewed tetrahedral elementary units. Supramolecular self-assembly of the tetrahedrally associated molecules from the bendable rod-like ferrocenomesogens allows the transfer of conformational chirality to a macroscopic level. Molecular modelling gave a satisfactory representation of the lattices to the experimental X-ray diffraction data.

Experimental Section

General Details: Reagent-grade chemicals and solvents were purchased from Aldrich (Yongin, Kyounggi-Do, Korea, Korea Branch) and TCI (Japan). Solvents were dried and freshly distilled before use. Melting points were determined by the capillary method with a Stuart Scientific apparatus SMP3. ^{1}H NMR spectra were recorded with a Bruker AM 400 spectrometer, *J* values are given in Hz. FTIR spectra were measured with a Nicolet Abatar-360 FTIR spectrometer from KBr tablets. Mass spectra were obtained with a JEOL JMS-AX505WA instrument by the FAB+ method in an *m*-NBA matrix by using an Xe^+ beam. Elemental analyses were performed with a Fisons instrument 2A1108 at the Korea Institute of

Science and Technology. DSC thermographs were obtained with a Perkin–Elmer Diamond microcalorimeter. Thermo-optical observations were carried out with a Nikon Eclipse E600 Pol optical polarized microscope equipped with a Mettler Toledo FP82 HT hot stage system and a Mettler FP90 central processor. Microphotographs were obtained with a Moticam 2300 digital camera. X-ray scattering measurements of **3a** were conducted with an apparatus consisting of an 18 kW rotating anode X-ray generator system (Rigaku Co.) operated at 46 kV × 20 mA, and mirror optics with point focusing. Cu-K_α radiation (λ = 1.5418 Å) from a 0.1 × 1 mm microfocus cathode was used. 2D diffraction patterns were recorded on imaging plates. The distance between sample and imaging plate was 68 cm for small-angle scattering and 18 cm for wide-angle scattering. The sample was held in an aluminum sample holder, which was sealed with windows of 7 μm Kapton films on both sides. The sample was heated with two cartridge heaters, and the temperature of the samples was monitored by a thermocouple placed close to the sample. X-ray scattering measurements for **1b**, **2** and **3b** were performed in transmission mode with synchrotron radiation of 1.5410 Å (E = 8.04 keV) and 1.5459 Å (E = 8.02 keV) at the 3C2 X-ray beam line at the Pohang Accelerator Laboratory, South Korea. Molecular models were obtained by using the program Hyperchem 7 from Hypercube, Inc. (Gainesville, Florida, USA).

Syntheses

1,1′-Bis[4-{2,3-difluoro-4-(*trans*-4-pentylcyclohexyl)phenyl}phenyl]-ferrocene (1a): A degassed solution of 1,1′-bis(4-bromophenyl)-ferrocene (70.4 mg, 0.143 mmol) was added to a stirred mixture of [2,3-difluoro-4-(*trans*-4-pentylcylohexyl)phenyl]boronic acid (100.1 mg, 0.323 mmol) and tetrakis(triphenylphosphane)-palladium(0) (20 mg, 0.0173 mmol) in toluene (20 mL) and aqueous sodium carbonate (2 M, 2.0 mL) under argon. The stirred reaction mixture was heated to reflux for 3 d. The completion of the reaction was monitored by TLC. The product was extracted into diethyl ether (2×), and the ethereal extracts were washed with water and dried with $MgSO_4$. After removal of the solvents by evaporation, the residue was placed on an Al_2O_3 column and eluted first with hexane and then with hexane/toluene (10:1). The first fraction with traces of the starting materials was rejected. The second fraction was collected and the solvents evaporated to dryness. Orange powder (33 mg, 27%). $C_{56}H_{62}F_4Fe$ (867): calcd. C 78.6, H 7.2; found C 78.5, H 7.2. MS: m/z = 867 [M^+]. IR: $\tilde{\nu}$ = 2923, 2851, 1595, 1504 (N–O), 1465, 1321 (N–O), 1111 (C–F), 892, 848, 815 cm^{-1}. ^1H NMR (400 MHz, $CDCl_3$, Me_4Si): δ = 7.30–7.20 (overlapped m, 8 H, C_6H_4), 7.02 (m, 2 H, $C_6H_2F_2$), 6.92 (m, 2 H, $C_6H_2F_2$), 4.57 (t, J = 1.8 Hz, 4 H, C_5H_4), 4.29 (t, J = 1.8 Hz, 4 H, C_5H_4), 2.85 (tt, J_{ae} = 3.0, J_{aa} = 12.3 Hz, 2 H, H_α), 1.90 (d, 8 H, CH_2), 1.49 (q, 4 H, CH_2), 1.50–1.20 (m, 18 H, CH_2 and H_β), 1.14 (q, 4 H, CH_2), 0.89 (t, 6 H, CH_3) ppm.

1,1′-Bis[2,3-difluoro-4-{4-(*trans*-4-decylcyclohexyl)phenyl}phenyl]-ferrocene (1b): Compound **1b** was synthesized as described above from 1,1′-bis(4-bromophenyl)ferrocene (0.141 g, 0.286 mmol) and [4-(*trans*-4-decylcylohexyl)-2,3-difluorophenyl]boronic acid (0.245 g, 0.644 mmol) in the presence of tetrakis(triphenylphosphane)palladium(0) (0.050 g, 0.0433 mmol) in toluene (28 mL) and aqueous sodium carbonate (2 M, 2.0 mL) under argon. Orange powder (0.088 g, 31%). $C_{66}H_{82}F_4Fe$ (1006): calcd. C 78.7, H 8.2; found C 78.8, H 8.3. MS: m/z = 1006 [M^+]. ^1H NMR (400 MHz, $CDCl_3$, Me_4Si): δ = 7.32–7.19 (overlapped m, 8 H, C_6H_4), 7.02 (m, 2 H, $C_6H_2F_2$), 6.92 (m, 2 H, $C_6H_2F_2$), 4.58 (t, J = 1.7 Hz, 4 H, C_5H_4), 4.29 (t, J = 1.7 Hz, 4 H, C_5H_4), 2.85 (tt, J_{ae} = 2.1, J_{aa} = 12.2 Hz, 2 H, H_α), 1.91 (m, 8 H, CH_2), 1.51 (m, 4 H, CH_2), 1.38–1.22 (m, 38 H, CH_2 and H_β), 1.20–1.00 (m, 4 H, CH_2), 0.89 (t, J = 6.4 Hz, 6 H ppm, CH_3) ppm.

1-[4-{4-(*trans*-4-Decylcyclohexyl)-2,3-difluorophenyl}phenyl]-1′-[4-(4-dodecyloxybenzaldimino)phenyl]ferrocene (2): Compound **2** was prepared according to a literature method.[9] Orange powder (55.9 mg, 84%). $C_{63}H_{79}F_2FeNO$ (960): calcd. C 78.8, H 8.3, N 1.5; found C 79.1, H 8.25, N 1.65. MS: m/z = 960 [M^+]. IR: $\tilde{\nu}$ = 2922, 2852, 1606 (C=N), 1560, 1522, 1508, 1459, 1384, 1247 (C–N), 1164, 1036, 890, 842, 817 cm^{-1}. ^1H NMR (400 MHz, $CDCl_3$, Me_4Si): δ = 8.33 (s, 1 H, CH=N), 7.77 (d, J_{AB} = 8.7 Hz, 2 H, C_6H_4), 7.31 (d, J_{AB} = 7.8 Hz, 2 H, C_6H_4), 7.27 (d, J_{AB} = 7.8 Hz, 2 H, C_6H_4), 7.22 (d, J_{AB} = 8.5 Hz, 2 H, C_6H_4), 7.11 (t, 1 H, $C_6H_2F_2$), 6.99 (d, J_{AB} = 8.5 Hz, 2 H, C_6H_4), 6.96 (d, J_{AB} = 8.7 Hz, 2 H, C_6H_4), 6.89 (t, 1 H, $C_6H_2F_2$), 4.54 (m, 4 H, C_5H_4), 4.27 (m, 4 H, C_5H_4), 4.02 (t, J = 6.6 Hz, 2 H, OCH_2), 2.79 (tt, J_{ae} = 3.0, J_{aa} = 12.3 Hz, 1 H, H_α), 1.89–1.79 (m, 6 H, OCHCH_2 and cyclohex), 1.52–1.20 (m, 39 H, CH_2 and H_β), 1.19–1.07 (m, 2 H, cyclohex), 0.90 (dt, J = 6.5 Hz, 6 H, CH_3) ppm.

1-[4-{4-(*trans*-4-Decylcyclohexyl)-2,3-difluorophenyl}phenyl]-1′-{4-[4-(4-dodecyloxybenzoyloxy)-2-hydroxybenzaldimino]phenyl}-ferrocene (3b): Compound **3b** was prepared according to a literature method.[9] Orange powder (65.5 mg, 89%). $C_{70}H_{83}F_2FeNO_4$ (1096): calcd. C 76.7, H 7.6, N 1.3; found C 76.55, H 7.6, N 1.4. MS: m/z = 1096 [M^+]. IR: $\tilde{\nu}$ = 3422 (OH), 2923, 2852, 1736 (C=O), 1618 (C=N), 1604, 1509, 1459, 1250 (C–N), 1169, 1147, 1116, 1060, 891, 844, 815 cm^{-1}. ^1H NMR (400 MHz, $CDCl_3$, Me_4Si): δ = 13.72 (s, 1 H, OH), 8.54 (s, 1 H, CH=N), 8.14 (d, J_{AB} = 8.8 Hz, 2 H, C_6H_4), 7.33 (d, J_{AB} = 8.5 Hz, 1 H, C_6H_3), 7.28 (d, J_{AB} = 8.5 Hz, 2 H, C_6H_4), 7.23 (d, J_{AB} = 8.5 Hz, 2 H, C_6H_4), 7.20 (d, J_{AB} = 8.5 Hz, 2 H, C_6H_4), 7.07 (m, 1 H, $C_6H_2F_2$), 7.04 (d, J_{AB} = 8.5 Hz, 2 H, C_6H_4), 6.98 (d, J_{AB} = 8.8 Hz, 2 H, C_6H_4), 6.91 (m, 1 H, $C_6H_2F_2$), 6.88 (d, J_{BX} = 2.2 Hz, 1 H, C_6H_3), 6.82 (dd, J_{AB} = 8.5, J_{BX} = 2.2 Hz, 1 H, C_6H_3), 4.58 (m, 4 H, C_5H_4), 4.31 (m, 4 H, C_5H_4), 4.05 (t, J = 6.5 Hz, 2 H, OCH_2), 2.78 (tt, J_{ae} = 3.0, J_{aa} = 12.2 Hz, 1 H, H_α), 1.85–1.79 (m, 6 H, OCH_2CH_2 and cyclohex), 1.60–1.20 (m, 39 H, CH_2 and H_β), 1.10 (m, 2 H, cyclohex), 0.89 (dt, J = 6.5 Hz, 6 H, CH_3) ppm.

Supporting Information (see footnote on the first page of this article): DSC thermograms of **1**–**3**.

Acknowledgments

This work was supported by the National Research Foundation of Korea (NRF) grant by the Korea government (MEST) No. 2011-0001129. We acknowledge the Pohang Accelerator Laboratory for providing the X-ray beam for XRD measurements.

[1] a) P. G. de Gennes, J. Prost, *The Physics of Liquid Crystals*, 2nd ed., Oxford University Press, New York, **1993**; b) G. W. Gray, V. Vill, H. W. Spiess, D. Demus, J. W. Goodby, *Physical Properties of Liquid Crystals*, Wiley-VCH, New York, **1999**; c) S. Chandrasekhar, *Liquid Crystals*, 2nd ed., Cambridge University Press, Cambridge, New York, **1992**; d) P. J. Collings, *Liquid Crystals: Nature's Delicate Phase of Matter*, 2nd ed., Princeton University Press, Princeton, **1990**.

[2] a) H. Kitzerow, C. Bahr, *Chirality in Liquid Crystals*, Springer, New York, **2000**; b) S. T. Lagerwall, *Ferroelectric and Antiferroelectric Liquid Crystals*, Wiley-VCH, New York, **1999**.

[3] a) D. Kondepudi, R. J. Kauffmann, N. Singh, *Science* **1990**, *250*, 975–976; b) J. Maclennan, M. Seul, *Phys. Rev. Lett.* **1992**, *69*, 2082–2085; c) R. Viswanathan, J. A. Zasadzinski, D. K. Schwartz, *Nature* **1994**, *368*, 440–443; d) J. Pang, N. A. Clark,

Phys. Rev. Lett. **1994**, *73*, 2332–2335; e) H. Koshima, *J. Mol. Struct.* **2000**, *552*, 111–116.

[4] a) S. I. Torgova, L. Komitov, A. Strigazzi, *Liq. Cryst.* **1998**, *24*, 131–141; b) K.-U. Jeong, D.-K. Yang, M. J. Graham, Y. Tu, S.-W. Kuo, B. S. Knapp, F. W. Harris, S. Z. D. Cheng, *Adv. Mater.* **2006**, *18*, 3229–3232; c) K.-U. Jeong, S. Jin, J. J. Ge, B. S. Knapp, M. J. Graham, J. Ruan, M. Guo, H. Xiong, F. W. Harris, S. Z. D. Cheng, *Chem. Mater.* **2005**, *17*, 2852–2865; d) K.-U. Jeong, B. S. Knapp, J. J. Ge, S. Jin, M. J. Graham, F. W. Harris, S. Z. D. Cheng, *Chem. Mater.* **2006**, *18*, 680–690.

[5] a) Y. Matsunaga, S. Miyamoto, *Mol. Cryst. Liq. Cryst.* **1993**, *237*, 311–317; b) T. Niori, T. Sekine, J. Watanabe, T. Furukawa, H. Takezoe, *J. Mater. Chem.* **1996**, *6*, 1231–1233; c) G. Pelzl, S. Diele, W. Weisflog, *Adv. Mater.* **1999**, *11*, 707–724; d) H. Takezoe, Y. Takanishi, *Jpn. J. Appl. Phys.* **2006**, *45*, 597–625; e) T. Sekine, T. Niori, J. Watanabe, T. Furukawa, S. W. Choi, H. Takezoe, *J. Mater. Chem.* **1997**, *7*, 1307–1309; f) C.-K. Lee, L.-C. Chien, *Ferroelectrics* **2000**, *243*, 231–237; g) S.-W. Choi, S. Kang, Y. Takanishi, K. Ishikawa, J. Watanabe, H. Takezoe, *Angew. Chem. Int. Ed.* **2006**, *45*, 6503–6506; h) V. Görtz, J. W. Goodby, *Chem. Commun.* **2005**, 3262–3264; i) D. R. Link, G. Natale, R. Shao, J. E. Maclennan, N. A. Clark, E. Körblova, D. M. Walba, *Science* **1997**, *278*, 1924–1927; j) D. M. Walba, E. Korblova, R. Shao, J. E. Maclennan, D. R. Link, M. A. Glaser, N. A. Clark, *Science* **2000**, *288*, 2181–2184.

[6] L. G. Fel, *Phys. Rev. E* **1995**, *52*, 702–717.

[7] a) L. Radzihovsky, T. C. Lubensky, *Europhys. Lett.* **2001**, *54*, 206–212; b) T. C. Lubensky, L. Radzihovsky, *Phys. Rev. E* **2002**, *66*, 031704 (1–27).

[8] a) H. R. Brand, H. Pleiner, P. E. Cladis, *Phys. A* **2005**, *351*, 189–197; b) H. R. Brand, H. Pleiner, P. E. Cladis, *Mol. Cryst. Liq. Cryst.* **2003**, *396*, 169–175; c) H. Pleiner, P. E. Cladis, H. R. Brand, *Eur. Phys. J. E* **2006**, *20*, 257–267; d) H. R. Brand, H. Pleiner, *Eur. Phys. J. E* **2010**, *31*, 37–49; e) L. Longa, G. Pająk, T. Wydro, *Phys. Rev. E* **2009**, *79*, 04701 (R1–4).

[9] O. N. Kadkin, E. H. Kim, S. Y. Kim, Y. J. Rha, J. Tae, M.-G. Choi, *Chem. Eur. J.* **2009**, *15*, 10343–10347.

[10] R. Knapp, M. Rehahn, *J. Organomet. Chem.* **1993**, *452*, 235–240.

[11] J. W. Goodby, M. A. Waugh, S. M. Stein, E. Chin, R. Pindak, J. S. Patel, *Nature* **1989**, *337*, 449–452.

[12] a) B. Mettout, *Phys. Rev. E* **2005**, *72*, 031706 (1–16); b) S. D. Peroukidis, P. K. Karahaliou, A. G. Vanakaras, D. J. Photinos, *Liq. Cryst.* **2009**, *36*, 727–737.

Received: February 19, 2011
Published Online: June 1, 2011

